



# High efficiency water splitting photoanodes composed of nano-structured anatase-rutile TiO<sub>2</sub> heterojunctions by pulsed-pressure MOCVD



Aleksandra J. Gardecka<sup>a</sup>, Catherine Bishop<sup>a</sup>, Darryl Lee<sup>b</sup>, Sacha Corby<sup>d</sup>, Ivan P. Parkin<sup>c</sup>, Andreas Kafizas<sup>d,\*</sup>, Susan Krumdieck<sup>a,\*</sup>

<sup>a</sup> Department of Mechanical Engineering, University of Canterbury, Christchurch, 8041, New Zealand

<sup>b</sup> Kott Technologies Limited, Christchurch, New Zealand

<sup>c</sup> Materials Chemistry Centre, Department of Chemistry, University College London, 20 Gordon Street, London, WC1H 0AJ, UK

<sup>d</sup> Department of Chemistry, Imperial College London, South Kensington, London, SW7 2AZ, UK

## ARTICLE INFO

### Keywords:

Titanium dioxide (TiO<sub>2</sub>)  
Anatase-rutile heterojunctions  
Solar water splitting  
Nanostructured photoelectrodes  
PP-MOCVD

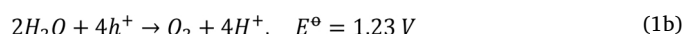
## ABSTRACT

In this article, thin solid films are processed via pulsed-pressure metal organic chemical vapour deposition (PP-MOCVD) on FTO substrates over a range of processing times to produce a range of thicknesses and microstructures. The films are highly nanostructured anatase-rutile TiO<sub>2</sub> composite films with unique single crystal dendrites. After annealing, carbon was removed, and materials showed improved water splitting activity; with IPCEs above 80% in the UV, photocurrents of  $\sim 1.2 \text{ mA cm}^{-2}$  at 1.23 V<sub>RHE</sub> at 1 sun irradiance and an extension of photoactivity into the visible range. The annealed material exhibits minimal recombination losses and IPCEs amongst the highest reported in the literature; attributed to the formation of a high surface area nanostructured material and synergistic interactions between the anatase and rutile phases.

## 1. Introduction

The extraction and combustion of more than 500 Gigatons of fossil carbon over the past 70 years has resulted in a build-up of CO<sub>2</sub> in the atmosphere that is causing global warming, and has driven research in alternative energy technologies that can ameliorate the effects of global warming [1,2]. Solar photovoltaic cells directly produce electricity from renewable, but intermittent solar radiation. The intermittency of increased solar and wind generation is driving the search for energy storage solutions [3]. Fujishima and Honda, first demonstrated water splitting on a TiO<sub>2</sub> photoelectrode using UV light [4]. Research on the photoelectrochemical water splitting has been focused on improving device efficiency, enhancing the utilization of visible spectrum radiation, and achieving commercial viability [5,6].

Photoelectrochemical water splitting is the process of decomposing water into oxygen and hydrogen on a semiconductor photocatalyst by light and an applied voltage [7]. The ultra-bandgap absorption of light results in the generation of electron hole pairs in the photocatalyst. The applied voltage assists the spatial separation of electron hole pairs, and these charge carriers participate in redox reactions at the semiconductor/electrolyte interface.



The conduction band should be sufficiently reducing for water reduction and hydrogen production to occur (Eq. (1a)). The valence band should be sufficiently oxidising for water oxidation and the formation of oxygen to occur (Eq (1b)) [8,9]. The bandgap of the material should be wide enough to surpass the thermodynamic potential for water splitting (1.23 V) and additional kinetic barriers [10,11].

Several research groups have focussed on improving the visible light activity and efficiency of water splitting materials [9,12]. One of the most common strategies for improving the efficiency is to introduce nanostructure, which decouples the problem of long light absorption depths and poor minority carrier diffusion lengths [13]. Hole carrier diffusion lengths in TiO<sub>2</sub> are on the order of 10's of nanometres [14], and for these carriers to reach the semiconductor/electrolyte interface and oxidise water, they need to be formed near the material surface. By introducing nanostructures, such as pillars and rods, more holes are formed near the surface of the material, and higher water splitting efficiencies have been demonstrated [15,16]. The studies to date have mainly used hydrothermal processing methods to synthesise TiO<sub>2</sub>-based photoelectrodes [15,17,18]. The clear gap in the research and development of efficient and viable photoanodes for solar hydrogen production is in the area of upscalable processing methods to robust and stable photoelectrode materials.

\* Corresponding authors.

E-mail addresses: [a.kafizas@imperial.ac.uk](mailto:a.kafizas@imperial.ac.uk) (A. Kafizas), [susan.krumdieck@canterbury.ac.nz](mailto:susan.krumdieck@canterbury.ac.nz) (S. Krumdieck).

In this paper we use a pulsed-pressure metal organic chemical vapour deposition (PP-MOCVD) method to produce nanostructured TiO<sub>2</sub> photoelectrodes from single-liquid source precursor solution of titanium tetra isopropoxide (TTIP) in toluene. Atmospheric pressure CVD is used to produce TiO<sub>2</sub> thin films during the float glass manufacture process, which has resulted in the commercialisation of numerous “self-cleaning” products including Activ™, Bioclean™, Sunclean™ and Variclean™ [19,20]. Control of precursor arrival rate and substrate temperature provides the control of microstructure [21]. In this study, we show that by controlling the deposition time by adjusting the number of pulses, we can produce a range of film thickness, fraction of anatase and rutile phases, and film topography.

In this article, we also study the role of co-deposited carbon, and its impact on the water splitting activity of our TiO<sub>2</sub> photoelectrodes. We find that highly nanostructured TiO<sub>2</sub> architectures, produced by pulsed-pressure metal organic chemical vapour deposition (PP-MOCVD), that contain both anatase and rutile phases, can achieve high water splitting efficiencies with minimal recombination losses (incident photon-to-current efficiencies up to 80% in the UV). We believe that this up-scalable synthetic route, and strategy for introducing nanostructure, can be applied to other materials systems that can harness more of the solar spectrum, and thus show potential enhancements in solar water splitting activity.

## 2. Experimental

### 2.1. Synthesis of TiO<sub>2</sub> photoanodes

TiO<sub>2</sub> films were grown using a pulsed pressure metal organic chemical vapour deposition (PP-MOCVD) process in a cold wall reactor, described previously by Lee et al. [22]. The deposition temperature was measured by k-type thermocouple inserted into the susceptor and heated by an induction coil. Depositions were carried out on F: SnO<sub>2</sub> TEC Glass™ (13 Ω/□; 13 mm × 6 mm × 18 mm). The temperature was maintained at 525 °C for the entirety of the deposition. A metered volume of precursor liquid solution (5 mol% solution of titanium tetra-isopropoxide (toluene, 500 μl per pulse) is directly injected through an ultrasonic atomizing nozzle into the continuously evacuated reactor volume at timed intervals, resulting in a sharp pressure pulse followed by pump-down. In the current reactor geometry, the susceptor is placed directly above an induction coil and the injector is located at the top of the reactor. The number of pulses was varied in each deposition resulting in films of varied thickness, anatase/rutile phase fractions and nanostructure (19, 92, 138, 184 and 460 pulses were investigated herein). The injection pulses were spaced 6 s apart. The chamber base pressure was held at 120 Pa, with the mean peak pressure in the region of 500 Pa. The effect of post-annealing was investigated, with samples annealed in air at 500 °C for 3 h.

### 2.2. Physical characterisation

X-ray diffraction (XRD) was carried out on the Bruker GADDS D8 diffractometer with a Cu K<sub>α</sub> X-ray source over the range 10° < 2θ < 66°. X-ray diffraction was carried out with a glancing incident angle of 1.0° unless otherwise stated. X-ray photoelectron spectroscopy (XPS) was carried out on a Thermo Scientific K-Alpha with a monochromatic Al-K<sub>α</sub> source. Survey scans were collected over the 0–1400 eV binding energy range with 1 eV resolution and a pass energy of 200 eV. Higher resolution scans (0.1 eV) encompassing the principal peaks of C (1s), O (1s), F (1s), Si (2p), and Ti (2p) were collected at a pass energy of 50 eV; with subsurface layers investigated by Ar-ion sputtering. Chemical environments were deconvolution using CasaXPS software [23], with the binding energies calibrated to graphitic carbon (1s = 285 eV) [24]. UV-vis absorption spectra were measured using a Shimadzu UV-vis 2600 spectrophotometer equipped with an integrating sphere over the wavelength range 190–1400 nm. Film

thickness and surface topographies were measured using scanning electron microscopy (SEM) on a JEOL 7000F Field Emission SEM at accelerating voltage of 15 keV. Film morphology was further studied using a Philips CM 200 transmission electron microscope (TEM), after a portion of the film was removed from the substrate using a diamond blade and applied onto a Cu grid and coated with carbon. Surface roughness was measured using a Digital Instruments Dimension 3100 atomic force microscope (AFM) operating in tapping mode with a scan frequency of 2 Hz over a 5 μm × 5 μm area. Results were processed using Gwyddion software [25].

### 2.3. Photoelectrochemical water splitting

All analyses were carried out in a home-made PEEK cell with quartz windows. The electrolyte was 1 M NaOH (Sigma Aldrich, 98%; pH = 13.6) in Milli-Q-water (Millipore Corp., 18.2 MΩ.cm at 25 °C). A three-electrode configuration was used, with a Pt mesh counter electrode, a Ag/AgCl/saturated-KCl reference electrode (0.197 V<sub>NHE</sub> at 25 °C; Metrohm) and the TiO<sub>2</sub> photoanode placed at the working electrode. An Autolab potentiostat (PGSTAT12 with an FRA2 module) was used to apply voltage and measure the current extracted from the sample. The applied voltages are reported vs the reversible hydrogen electrode (V<sub>RHE</sub>), converted using the Nernst equation:

$$V_{RHE} = V_{Ag/AgCl} + 0.0591 \times pH + V_{Ag/AgCl}^\theta \quad (2)$$

Current-voltage curves were measured from 0.0 to 2.0 V<sub>RHE</sub> at a scan rate of 40 mV s<sup>-1</sup>. A 365 nm LED light was used as the excitation source (LZ1-10U600, LedEngin. Inc.). The light intensity (~44 mW cm<sup>-2</sup>) was measured using an optical power meter (PM 100, Thorlabs) with a power sensor (S120UV, Thorlabs). The incident photon to current efficiency (IPCE) was measured at a fixed potential of 1.23 V<sub>RHE</sub> (the thermodynamic potential for water oxidation) using an ozone-free xenon lamp (75 W, Hamamatsu) coupled to a monochromator (OBB-2001, Photon Technology International) over the wavelength range 250–425 nm. The IPCE was calculated using the following equation:

$$IPCE(\%) = \frac{I_{ph} \times 1239.8}{P_{mono} \times \lambda} \times 100 \quad (3)$$

where  $I_{ph}$  (mA cm<sup>-2</sup>) is the photocurrent, 1239.8 (eV nm) is a product of Planck's constant with the speed of light,  $P_{mono}$  (mW cm<sup>-2</sup>) is the power and  $\lambda$  (nm) is the wavelength of the monochromated light. Sample stability was also measured at a fixed potential of 1.23 V<sub>RHE</sub> under chopped 365 nm LED light for 1 h.

The solar water splitting activity was simulated from IPCE measurements. This theoretical solar photocurrent (TSP) was determined by multiplying the IPCE with the AM1.5 solar spectrum, and then converting this into a current:

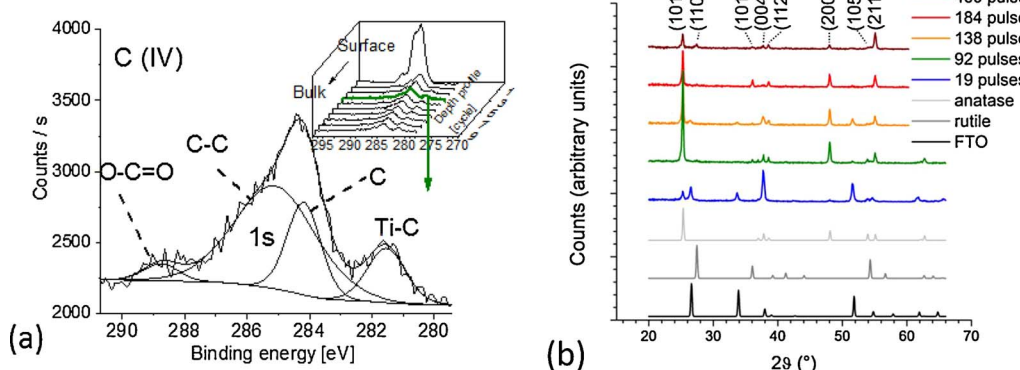
$$TSP(mA \cdot cm^{-2}) = \int_{300nm}^{280nm} IPCE \times AM1.5(photon \cdot cm^{-2}) \times 1000/1C \quad (4)$$

where 1C is  $6.241 \times 10^{18}$  electrons per second.

## 3. Results and discussion

### 3.1. Physical characterisation

TiO<sub>2</sub> thin films were grown on FTO glass substrates using a PP-MOCVD process. With the exception of the thinnest film (19 deposition pulses), as-deposited films were brown/black in appearance (92–460 pulses). XPS showed that these thicker TiO<sub>2</sub> films contained high levels of carbon (typically between 3–7 at.% as calculated from XPS depth profiles). Ar-ion sputtering was used to etch away surface layers, and the carbon 1 s environment was investigated from the surface into the material bulk (Fig. 1a). Adventitious carbon was observed at the



material surface [26]. Ar-ion sputtering removed this adventitious carbon, and revealed a new environment ( $\sim 281.5$  eV) associated with ion induced Ti-C bonding [27]. This type of bonding was observed by Galuska et al. on titanium films grown on carbon. Ar-ion sputtering also revealed a carbon environment at  $\sim 284.2$  eV, that has been attributed to the presence of highly ordered carbon layers [28]. Surface XPS analysis of the Ti 2p environment revealed a binding energy for the Ti  $2p_{3/2}$  environment of  $\sim 458.7$  eV (Fig. S1a), which corresponds to Ti<sup>4+</sup> in TiO<sub>2</sub> [29]. No indication of Ti<sup>3+</sup> formation was observed. After annealing in air, the surface carbon content in the 184 pulse sample decreased substantially from  $\sim 11$  at.% to  $\sim 5$  at.% (Fig. S2).

XRD of the as-deposited samples showed that the thinnest film (19 pulses) was composed of anatase, and that thicker samples contained both anatase and rutile phases of TiO<sub>2</sub> (Fig. S1b). No diffraction peaks were observed in the XRD pattern of the as-deposited thickest sample (420 pulses); however, after annealing in air, and the subsequent removal of carbon, both anatase and rutile peaks were observed (Fig. 1b). The anatase: rutile phase fraction was estimated using a refined scale factor, which was determined from the sum total peak counts of each phase (Equation S1) [30]. Rutile content was low, and ranged between 0 and 9% across all samples (Table S1). Interestingly, thicker samples showed higher levels of rutile, where the rutile content increased from 2% in the post-annealed 92 pulse sample to 9% in the post-annealed 460 pulse sample. The XRD of the 184 pulse sample was also measured at various glancing incidence angles (Fig. S3). The peak height ratio of anatase (101) to rutile (110), at various glancing incidence angles (0.2–1.4°), did not vary substantially. Shallow incidence angles primarily probe the surface of the material and steeper incidence angles probe further into the material bulk. Our results showed that the anatase/rutile phase fraction did not change with material depth.

UV-vis absorption spectroscopy of the post-annealed 19 pulse sample revealed a band edge at  $\sim 380$  nm (Fig. 2). There was no significant difference in the UV-vis absorption spectrum of the 19 pulse sample before and after annealing, which we attribute to the lack of carbon incorporated into these films. A Tauc plot showed that the bandgap of the 19 pulse sample was  $\sim 3.1$  eV (Fig. S4), similar to literature values for anatase TiO<sub>2</sub> ( $\sim 3.2$  eV) [31,32]. UV-vis absorption spectroscopy of the as-deposited 92 pulse sample revealed a red-shifted band edge at  $\sim 410$  nm, alongside strong absorption into the visible (Fig. 2). The strong absorption in the visible was due to a high concentration of carbon present in this material. This was typical of thicker samples made from a higher number of deposition pulses, which all appeared brown/black in colour. However, after annealing in air, the 92 pulse sample maintained its red-shifted band edge and showed a decrease in absorption in the visible. This decrease in visible light absorption was attributed to the removal of carbon by annealing, resulting in a colour change to hazy white (Fig. 2, inset). After annealing, the 92 pulse sample possessed a higher degree of visible light “absorption” compared with the thinner 19 pulse sample. Primarily, this was not due to light absorption, but rather, an increase in the diffuse scattering of

**Fig. 1.** (a) XPS of the carbon 1s binding energy environment in the as-deposited TiO<sub>2</sub> sample made from 184 pulses (inset shows depth profile) and (b) XRD spectra of the air-annealed TiO<sub>2</sub> samples (19–460 pulses), alongside anatase, rutile and FTO powder standards. Miller indices correspond to anatase (non-asterisked) and rutile (asterisked) phases.

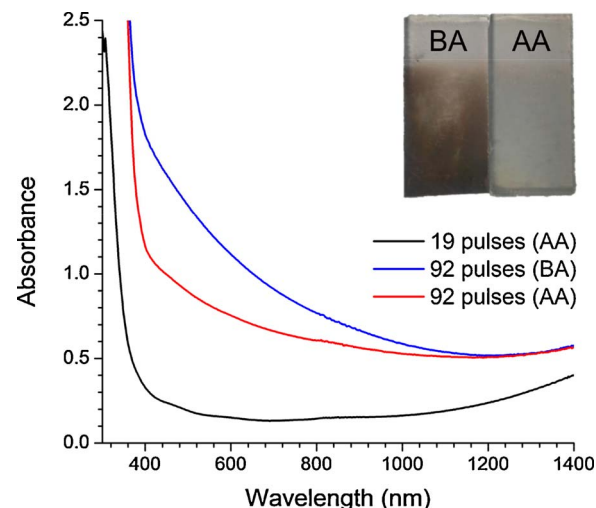


**Fig. 2.** UV-vis absorption spectroscopy of the 19 pulse sample after annealing (AA), and the 92 pulse sample before annealing (BA) and after annealing (inset shows a photograph of the 92 pulse sample before and after annealing).

light (which gave rise to a false positive of visible light absorption). This was caused by an increase in surface roughness in thicker films, and the resulting formation of surface nanostructures, as evidenced by SEM (Fig. 3).

SEM was used to investigate the topography and thickness of the samples (Fig. 3). Film thickness increased from  $\sim 100$  nm in the 19 pulse sample to  $\sim 11$   $\mu\text{m}$  in the 460 pulse sample. This increase in film thickness was not linear with the number of deposition pulses; with the growth rate increasing exponentially with the number of pulses ( $\sim 5$ ,  $\sim 6$ ,  $\sim 14$  and  $\sim 23$  nm per pulse for the 19, 92, 184 and 460 pulse samples respectively). The 19 pulse sample consisted of randomly organised crystallites. The 92 pulse sample consisted of nanostructured protruding rounded structures. The thicker films (184 and 460 pulses) consist of nanostructured dendrites of larger diameter in thicker films. No substantial change in microstructure or film thickness was observed after annealing the samples in air (Fig. S5).

AFM was also used to investigate the surface topography of all samples (Fig. S6). Both surface area and surface roughness increased with film thickness (Table 1). The surface area, per geometric  $25 \mu\text{m}^2$ , increased from  $36.0 \mu\text{m}^2$  in the 19 pulse sample to  $56.3 \mu\text{m}^2$  in the 460 pulse sample and the root mean square (RMS) roughness increased from  $42.3 \text{ nm}$  in the 19 pulse sample to  $257 \text{ nm}$  in the 460 pulse sample. No significant change in surface area or surface roughness was observed after annealing in air (Fig. S7).

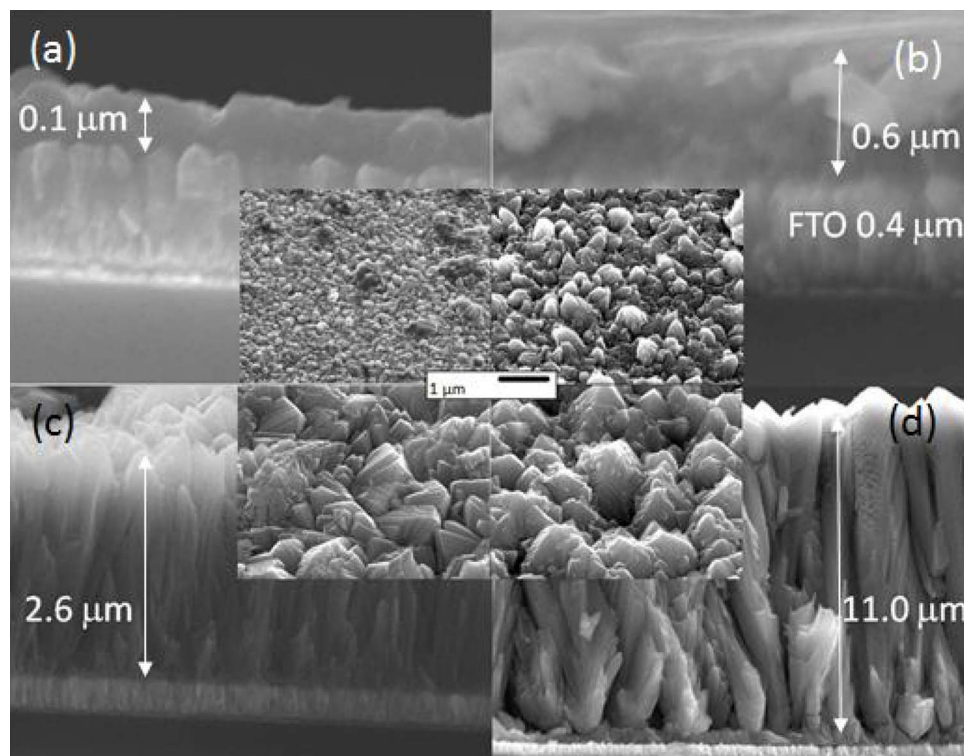


**Fig. 3.** Side-on cross-sectional SEM images of  $\text{TiO}_2$  samples, after annealing in air, made from (a) 19, (b) 92, (c) 184 and (d) 460 pulses (inserts in the centre show top-down images of surface topography). Arrows indicate mean film thickness.

**Table 1**

Summary of the physical properties and water splitting performance of our  $\text{TiO}_2$  photoelectrodes, after being annealed in air.

Sample (number of pulses)	Surface area per geometric (number of pulses)	RMS roughness (nm)	Film thickness ( $\mu\text{m}$ )	Photocurrent ( $\text{mA}\cdot\text{cm}^{-2}$ ) – 365 nm light (~44 mW $\text{cm}^{-2}$ ) <sup>a</sup>	IPCE at 350 nm (%) <sup>a</sup>
19	36.0	42.3	0.1	1.4	32
92	32.6	97.1	0.6	4.6	85
182	41.1	123	2.6	3.5	39
460	56.3	257	11.0	3.9	40

<sup>a</sup> When held at 1.23 V<sub>RHE</sub> and irradiated from the front (semiconductor-electrolyte interface).

### 3.2. $\text{TiO}_2$ microstructure

Fragments scraped from the 184 pulse sample contained crystallite fragments that could be imaged by TEM, which showed that these fragments were primarily composed of anatase dendrites (Fig. 4). The approximate length and width of each dendrite arm was 70 nm and 10–20 nm, respectively. High resolution imaging reveals lattice fringes with spacing corresponding to anatase (101) planes. These anatase (101) planes were perpendicular to the dendrite fragment lying flat on the TEM grid, but the plane of the fragment could not be identified here. Fringes corresponding to rutile crystals, observed by XRD, were not observed by TEM analysis. No carbon structures were found in the TEM analysis suggesting that carbon forms thin layers at crystallite interfaces only, which can also account for lack of structural changes in the film before and after annealing as seen in Fig. S5 and Fig. S7.

Dendritic films of anatase  $\text{TiO}_2$  have been grown using a number of synthesis routes and various explanations have been given for their formation, focusing mostly on deposition conditions [33–36]. Takahashi et al. reported both anatase and mixed phase anatase/rutile  $\text{TiO}_2$  films deposited at 500 °C using TTIP [35]. Only anatase growth was observed at low carrier gas flows ( $\text{N}_2$ , 0.2  $\text{cm}^3\text{s}^{-1}$ ), whereas rutile content increased exponentially with an increase in flow rate. Similar

nanostructures were observed by Takahashi et. al., to the dendrites observed herein, however no TEM analysis was presented and nanoscale features were not described [35]. Biswas et al. showed that nanoscale anatase columns with (112) texture and widths of approximately 20–30 nm could be grown by aerosol-assisted CVD at 500 °C [18,37,38]. Goossens et al. [34] reported nanostructured dendritic anatase films, with a similar morphology to Takahashi et. al.'s [35], deposited using APCVD from mixtures of TTIP and  $\text{TiCl}_4$  in the temperature range of 300–350 °C. The water splitting activity of dendritic titania, grown using the aforementioned CVD processes, have not previously been examined.

### 3.3. Photoelectrochemical water splitting

The photoelectrochemical water splitting activity of our  $\text{TiO}_2$  photoelectrodes was examined, both before and after being annealed in air. Current voltage curves were measured in 1 M NaOH (pH = 13.6), sweeping the voltage from 0.0 to 2.0 V<sub>RHE</sub>. A 365 nm LED (~44 mW  $\text{cm}^{-2}$ ) was turned on and off, roughly every second. The current-voltage curves, measured under front irradiation, are shown in Fig. 5 for a series of samples made from a range of deposition pulses. We will first discuss the performance of as-deposited samples, before they were annealed in air. The 19 pulse sample, which possessed the least nanostructure and consisted solely of the anatase phase, showed the earliest photocurrent onset (~0.1 V<sub>RHE</sub>) and plateau (~0.8 V<sub>RHE</sub>), and showed a photocurrent of ~1.4 mA  $\text{cm}^{-2}$  at 1.23 V<sub>RHE</sub>. The 92 pulse sample, which possessed dendritic nanostructure and was composed of a mixture of anatase and rutile phases, showed a similarly early photocurrent onset but plateaued later (~1.3 V<sub>RHE</sub>). The 92 pulse sample showed a photocurrent of ~2.4 mA  $\text{cm}^{-2}$  at 1.23 V<sub>RHE</sub>. A decrease in photoelectrochemical performance was observed in thicker materials, the 184 and 460 pulse samples showing photocurrents of ~1.4 mA  $\text{cm}^{-2}$  and ~0.1 mA  $\text{cm}^{-2}$  at 1.23 V<sub>RHE</sub> respectively. We will now discuss the performance of samples after being annealed in air. The 19 pulse sample showed no significant change to its performance before being annealed. However, the 92 pulse sample showed substantial improvements in performance, where the photocurrent onset shifted

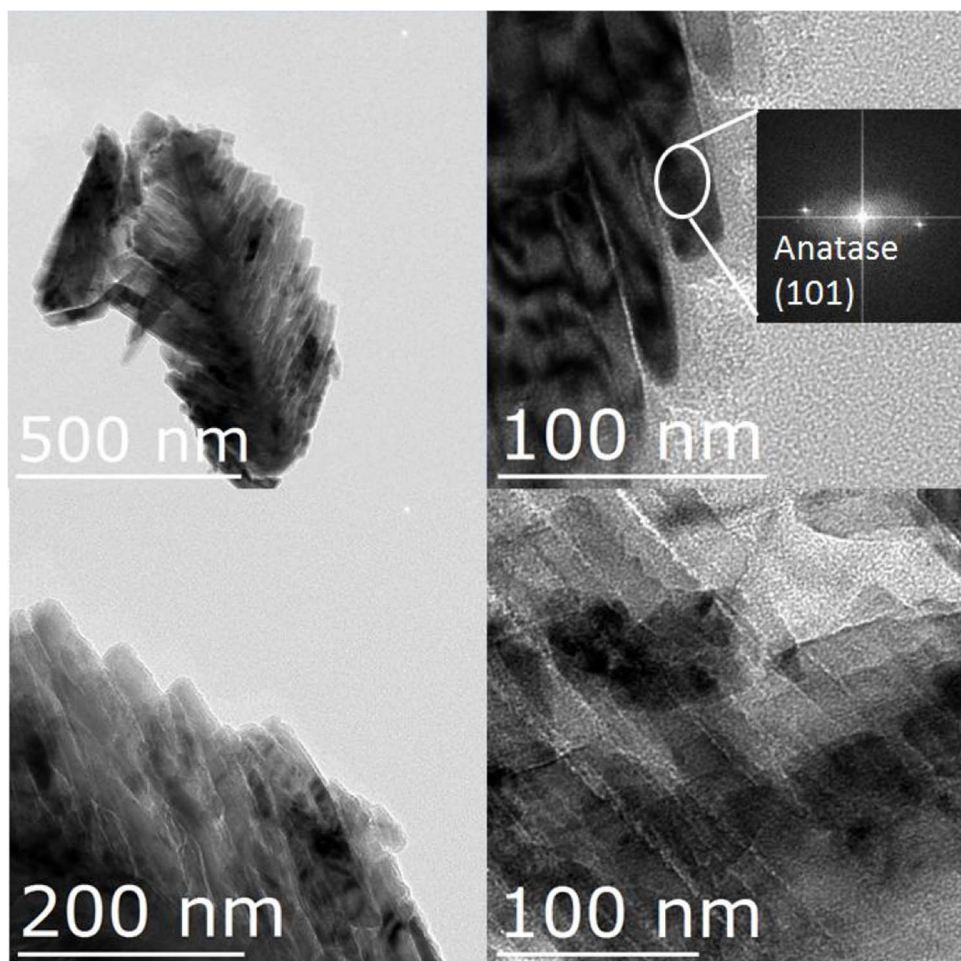


**Fig. 4.** TEM micrographs of the as-deposited  $\text{TiO}_2$  sample grown from 184 pulses. Measurement of the d-spacing (top right) showed that these crystals were anatase  $\text{TiO}_2$  single crystals.

cathodically to  $\sim 0.1 \text{ V}_{\text{RHE}}$ , the photocurrent plateaued earlier ( $\sim 1.0 \text{ V}_{\text{RHE}}$ ) and the photocurrent increased substantially; reaching  $\sim 4.6 \text{ mA cm}^{-2}$  at  $1.23 \text{ V}_{\text{RHE}}$ . Similar enhancements in photoelectrochemical water splitting activity were observed in the 184 and 460 pulse samples; reaching  $\sim 3.5 \text{ mA cm}^{-2}$  and  $\sim 3.9 \text{ mA cm}^{-2}$  at  $1.23 \text{ V}_{\text{RHE}}$  respectively. Turning our attention to the photoelectrochemical performance when irradiated from the back (Fig. S8), we find similar trends to what was observed under front irradiation, both before and after being annealed in air, with the exception that the thickest sample (460 pulses) showed the highest activity.

IPCEs were measured under front irradiation at a constant applied potential of  $1.23 \text{ V}_{\text{RHE}}$ , both before and after being annealed in air (Fig. 6). Before annealing, there was a clear trend in activity, where the thinnest sample (19 pulses) showed higher light conversion efficiencies,

and increases in film thickness resulted in lower efficiencies. Intriguingly, all samples showed a sharp cut-off in activity above  $375 \text{ nm}$ , despite thicker samples containing a significant rutile component ( $E_{\text{bg}} \sim 3.0 \text{ eV}$ ,  $\sim 410 \text{ nm}$ ) and a more red-shifted band edge (Fig. 2). This indicated that only the anatase component was active in splitting water for non-annealed films ( $E_{\text{bg}} \sim 3.2 \text{ eV}$ ,  $\sim 388 \text{ nm}$ ). Post-annealing, the 92 pulse sample showed a dramatic increase in activity, matching the light conversion efficiencies of the 19 pulse sample in the UV-region ( $250$ – $300 \text{ nm}$ ), and also showing extended activity into the visible. Post-annealing, thicker samples, which contained a rutile component, showed higher visible light activities than the thinnest sample (19 pulses), which solely contained anatase. When irradiating the samples from the back (*i.e.* through the FTO layer), a loss in UV activity from  $250$  to  $325 \text{ nm}$  was observed (Fig. S9). This was attributed to UV

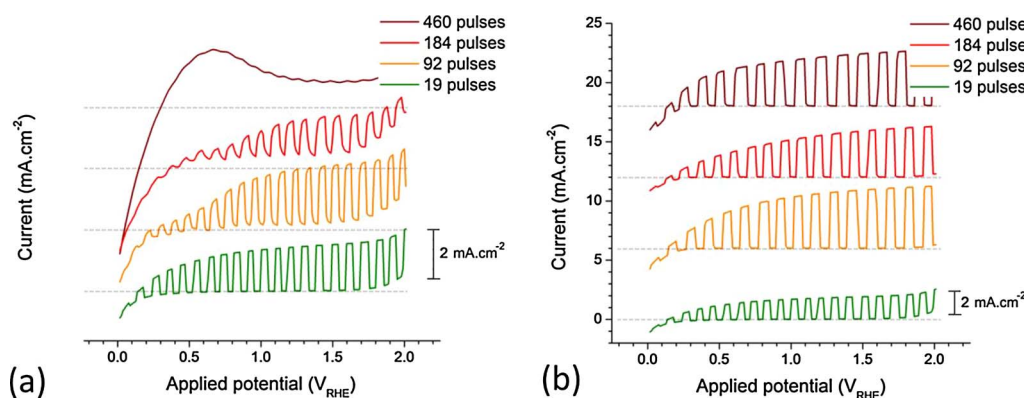
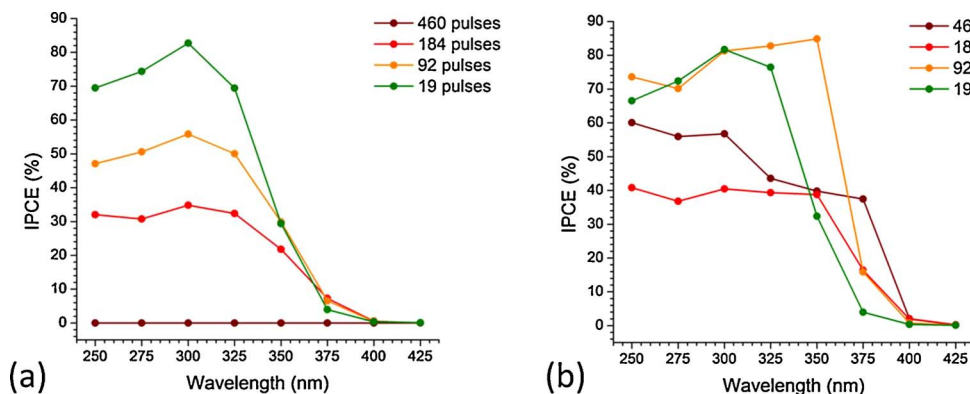


**Fig. 5.** Current-voltage curves for a series of  $\text{TiO}_2$  samples measured under front irradiation (a) before and (b) after being annealed in air. Samples were measured in  $1 \text{ M NaOH}$  ( $\text{pH} = 13.6$ ), the current was swept from  $0.0$  to  $2.0 \text{ V}_{\text{RHE}}$  at a scan rate of  $40 \text{ mV s}^{-1}$  and a  $365 \text{ nm}$  LED ( $\sim 44 \text{ mW cm}^{-2}$ ) was turned on and off roughly every second. Dotted grey lines represent the zero-line of current flow for each sample (*i.e.*  $0 \text{ mA cm}^{-2}$ ).



absorption by the FTO layer, which blocked UV light from reaching the  $\text{TiO}_2$  layer. Similar trends in light conversion behaviour were observed, pre and post-annealing, to those found under front irradiation; with the exception that the thickest sample (460 pulses) showed the highest activity. Of note, the  $\text{TiO}_2$  photoelectrodes grown herein were durable, and showed no change in photocurrent over a period of testing for one hour (Fig. S10).

Looking at general trends in photoelectrochemical activity, thinner samples were more active than thicker samples before being annealed. However, after annealing, thicker samples showed substantial increases in activity; both under 365 nm irradiation (Fig. 5) and into the visible (Fig. 6). This was attributed to two complimentary physical properties: (i) an increased nanostructure and (ii) the activation of the rutile component. We will discuss each point in turn.

An increase in nanostructure is often beneficial for photoelectrochemical water splitting systems, and is attributed to the enhancement of light absorption near the semiconductor/electrolyte interface (as opposed to the bulk). This is of particular importance in  $\text{TiO}_2$ , where the hole diffusion length is on the order of 10's of nanometres [14]. On the other hand, given the long diffusion length of electrons in  $\text{TiO}_2$ , on the order of several micrometers [39], electron extraction into the FTO layer is possible, so long as film thickness does not surpass this diffusion limit. Of note, this electron diffusion limit was likely surpassed by our thickest sample (460 pulses,  $\sim 11 \mu\text{m}$ ), and as a consequence, showed higher light conversion efficiencies under back irradiation (Fig. S9) than front irradiation (Fig. 6). Thicker, and more nanostructured photoelectrodes, often show higher levels of activity than thinner and more flat-structured photoelectrodes, as they better utilise light that is absorbed deeper into the material (*i.e.* wavelengths at the band edge, that are not absorbed as strongly as wavelengths lower than the band edge). In addition to this, nanostructured materials scatter light more effectively than flatter structures, and have been used to good effect in enhancing the performance of photovoltaic devices [40,41].

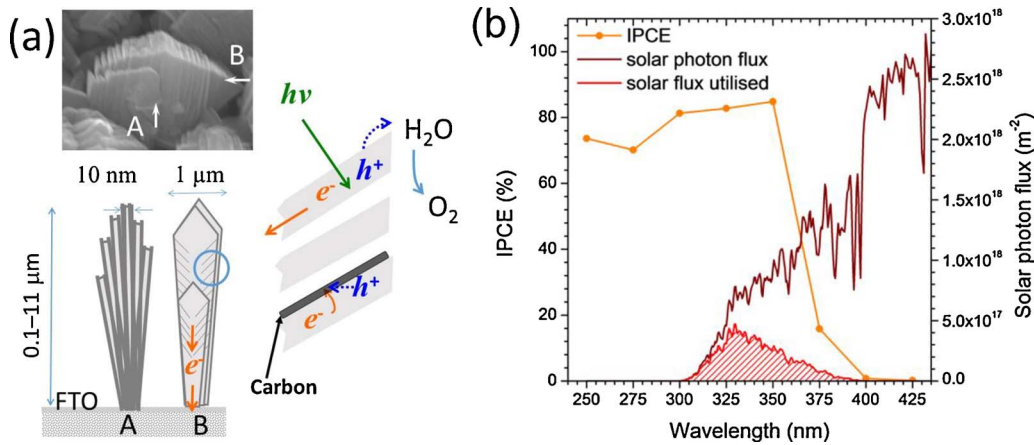


Fig. 6. IPCE measured at a constant applied potential of 1.23 V<sub>RHE</sub> in 1 M NaOH (pH = 13.6) for a series of  $\text{TiO}_2$  samples under front irradiation (a) before and (b) after annealing.

Rutile was found more prominently in thicker samples (92–460 pulse depositions), and upon annealing, the water splitting activity was extended into the near-visible (Fig. 6). This was due to the “activation” of the rutile component upon annealing. It was not that annealing resulted in an increase in rutile formation in our materials (as evidenced by our XRD studies, see Table S1), but rather, it was the removal of carbon through annealing that resulted in the activation of rutile already present in our materials (Fig. S2). This was because carbon was an inhibitor, which prevented electron extraction from our materials, and inhibited the performance of rutile more so than anatase. In the 92 pulse sample, annealing resulted in a synergic interaction between the anatase and rutile phases, matching the UV light conversion efficiencies of the 19 pulse sample (*i.e.* pure anatase) and showing extended activity into the visible. Synergic interactions in anatase: rutile composites are frequently observed, where in fact, P25 Degussa  $\text{TiO}_2$ , a commercially available powder composite composed of both anatase and rutile phases, is often considered the benchmark photocatalyst given its high activity for a range of photocatalytic processes; including water splitting) [30]. The physical properties and water splitting activities of our  $\text{TiO}_2$  photoelectrodes, after being annealed in air, is shown in Table 1.

We will now turn our attention to the role of carbon in relation to the water splitting activity of our  $\text{TiO}_2$  photoelectrodes. As-deposited samples, grown from 92 to 460 deposition pulses, possessed high levels of carbon (typically between 3 and 7 at.-%). Carbon has a work function of  $\sim 4.8 \text{ eV}$  [42], and would thus possess a Fermi level of  $\sim 0.3 \text{ V}_{\text{RHE}}$ . As the conduction band potentials of anatase and rutile are more negative than this Fermi level [30]. There is a thermodynamic driving force for photo-generated electrons to move into carbon sites. Our XPS and TEM analyses indicated carbon grew mostly in sheets, located between dendritic anatase crystals. As such, there is likely no consistent or interconnected carbon structure that runs through the  $\text{TiO}_2$  structure. This means that photo-generated electrons, which move into carbon sites,

Fig. 7. (a) A cartoon that describes how sheets of carbon form between  $\text{TiO}_2$  crystals, and how the material functions in photocatalytically splitting water under a positive applied potential and ultra-bandgap light. (b) The theoretical solar photocurrent determined for the 92 pulse sample under front irradiation.

**Table 2**

Summary of the phases, structures, synthesis routes and water splitting performances of example TiO<sub>2</sub>-based photoelectrodes in the literature, as compared with our best performing material (the 92 pulse sample, post annealing in air).

Synthetic route	Phase	Architecture	IPCE at 350 nm (%) <sup>a</sup>	Photocurrent (mA·cm <sup>-2</sup> ) at 1 sun irradiance <sup>a</sup>	reference
PP-MOCVD	anatase: rutile	dendritic	85	~1.2	herein
Aerosol-assisted CVD	anatase	cauliflower-structured	n/a	~0.2	[44]
Hydrothermal	rutile	branched nanorods	~32	~0.85	[36]
Hydrothermal	anatase: rutile	rutile nanorods; anatase branches	~57	~1.1	[43]

<sup>a</sup> When held at 1.23 V<sub>RHE</sub> and irradiated from the front (semiconductor-electrolyte interface).

are likely trapped within these isolated carbon sheets; increasing the likelihood of electron-hole recombination (Fig. 7a). This was evidenced in our current-voltage curves, where dark current capacitance was observed; increasingly so in thicker films. Moreover, thicker films showed lower photocatalytic activities under front irradiation than thinner films (Fig. 5b), in addition to a slower rise in photocurrent when the light was turned on, which we attribute to slower electron extraction kinetics due to the inhibiting role of carbon. However, after annealing the samples in air at 500 °C, carbon was oxidised and removed, resulting in substantially higher water splitting activity (Figs. 5 and 6). Although carbon inhibits water splitting in our TiO<sub>2</sub> photoelectrodes, our physical characterisations indicate carbon templates the growth of dendritic TiO<sub>2</sub> nanostructures; essential for enhancing the water splitting activity of TiO<sub>2</sub>-based photoelectrodes [43]. This, coupled with the fact that carbon can be easily removed by annealing, shows that it may serve as a tool for creating nanostructured water splitting devices.

Theoretical solar photocurrent (TSP) was determined by multiplying IPCE spectra with the AM 1.5 solar spectrum (Eq. (4)). Our most active sample under front irradiation (92 pulses) showed a TSP of ~1.2 mA cm<sup>-2</sup> at 1.23 V<sub>RHE</sub> under 1 sun irradiance (Fig. 7b), and is compared with TiO<sub>2</sub>-based photoelectrodes from the literature (Table 2). Wijayantha et al. grew cauliflower-structured anatase TiO<sub>2</sub> photoelectrodes using an aerosol-assisted CVD route [44]. These photoelectrodes showed photocurrents of ~0.2 mA cm<sup>-2</sup> at 1.23 V<sub>RHE</sub> under 1 sun irradiance (100 mW cm<sup>-2</sup>, Xe lamp). Zheng et al., using hydrothermal methods, grew hierarchically branched single crystal rutile nanorods [36]. These photoelectrodes showed light conversion efficiencies near 70% at 380 nm and photocurrents of ~0.83 mA cm<sup>-2</sup> at 0.8 V<sub>RHE</sub> under near 1 sun irradiance (88 mW cm<sup>-2</sup>, Xe lamp). Gu et al. grew nanostructured TiO<sub>2</sub> photoelectrodes using a two-step hydrothermal method, in which highly oriented rutile nanorods were grown and decorated with anatase branches [43]. These photoelectrodes showed light conversion efficiencies above 60% in the UV region, and photocurrents of ~1.0 mA cm<sup>-2</sup> at 0.8 V<sub>RHE</sub> under 1 sun irradiance (100 mW cm<sup>-2</sup>, Xe lamp). Comparing the literature, the photoelectrodes synthesised herein using CVD show similar water splitting activities to some of the leading TiO<sub>2</sub>-based materials. Given CVD is an economically viable and upscalable process, which is currently used to grow self-cleaning TiO<sub>2</sub> coatings on mass scale (e.g. Pilkington NSG Activ), this article should serve as a model example for upscalably growing nanostructured photoelectrodes made from visible-light active materials that can harness a greater portion of sunlight.

#### 4. Conclusions

The photoelectrochemical water oxidation performance of nanostructured anatase, and anatase-rutile TiO<sub>2</sub> photoelectrodes was investigated; as well as the role of co-deposited carbon. Highly nanostructured architectures were produced by an upscalable CVD route (PP-MOCVD), where the deposition parameters could be varied to fine-tune several material properties such as: (i) film thickness, (ii) the anatase-rutile phase fraction, and (iii) topography.

Photoelectrodes that contained both the anatase and rutile phases showed synergistic enhancements in activity, compared with anatase

alone, with incident photon-to-current efficiencies above 80% in the UV region, and photocurrents of ~1.2 mA cm<sup>-2</sup> at 1.23 V<sub>RHE</sub>. We propose that co-deposited carbon might play a role in templating the growth of dendritic nanostructures. Although carbon inhibited water splitting in this system, it could be removed by a post-deposition annealing process, resulting in highly active and nanostructured photoelectrodes. We believe that this article should serve as a model example for the upscalable growth of highly active nanostructured photoelectrodes, where similar design principles should be applied to more visible-light materials to realise enhanced solar activity.

#### Acknowledgments

This work is supported by New Zealand Ministry for Business, Innovation and Employment under the High Value Manufacturing Science and Technology Research Program Contract No. CONT-42986-HVMSTR-UOC (UOCX1501) and a research contract from KOTI Technologies Limited. I.P.P. thanks the Engineering and Physical Sciences Research Council (EPSRC) for their financial support (EP/L015862/1). A.K. thanks Imperial College for a Junior Research Fellowship.

#### Appendix A. Supplementary data

Supplementary data associated with this article can be found, in the online version, at <http://dx.doi.org/10.1016/j.apcatb.2017.11.033>.

#### References

- [1] W.S. Broecker, Climatic change are we on the brink of a pronounced global warming? *Science* 189 (1975) 460–463.
- [2] N. Gruber, Warming up, turning sour, losing breath: ocean biogeochemistry under global change, *Philos Trans A Math. Phys. Eng. Sci.* 369 (2011) 1980–1996.
- [3] B.K. Sovacool, The intermittency of wind, solar, and renewable electricity generators: technical barrier or rhetorical excuse? *Utilities Policy* 17 (2009) 288–296.
- [4] A. Fujishima, K. Honda, Photolysis-decomposition of water at the surface of an irradiated semiconductor, *Nature* 238 (1972) 37–38.
- [5] F.E. Osterloh, Inorganic materials as catalysts for photochemical splitting of water, *Chem. Mater.* 20 (2008) 35–54.
- [6] F.E. Osterloh, Inorganic nanostructures for photoelectrochemical and photocatalytic water splitting, *Chem. Soc. Rev.* 42 (2013) 2294–2320.
- [7] A.L. Linsebigler, G. Lu, J.T. Yates Jr., Photocatalysis on TiO<sub>2</sub> surfaces: principles, mechanisms, and selected results, *Chem. Rev.* 95 (1995) 735–758.
- [8] A. Fujishima, T.N. Rao, D.A. Tryk, Titanium dioxide photocatalysis, *J. Photochem. Photobiol. C: Photochem. Rev.* 1 (2000) 1–21.
- [9] Y. Li, Y.-L. Li, B. Sa, R. Ahuja, Review of two-dimensional materials for photocatalytic water splitting from a theoretical perspective, *Catal. Sci. Technol.* 7 (2017) 545–559.
- [10] J.R. Bolton, S.J. Strickler, J.S. Connolly, Limiting and realizable efficiencies of solar photolysis of water, *Nature* 316 (1985) 495–500.
- [11] A. Kafizas, Y. Ma, E. Pastor, S.R. Pendlebury, C. Mesa, L. Francàs, F. Le Formal, N. Noor, M. Ling, C. Sotelo-Vazquez, The water oxidation kinetics of accumulated holes on the surface of a TiO<sub>2</sub> photoanode: a rate law analysis, *ACS Catal.* 7 (2017) 4896–4903.
- [12] S.J. Moniz, S.A. Shevlin, D.J. Martin, Z.-X. Guo, J. Tang, Visible-light driven heterojunction photocatalysts for water splitting—A critical review, *Energy Environ. Sci.* 8 (2015) 731–759.
- [13] A. Kafizas, R. Godin, J.R. Durrant, Charge carrier dynamics in metal oxide photoelectrodes for water oxidation, *Semicond. Semimetals* 97 (2017) 3–46.
- [14] P. Salvador, Hole diffusion length in n-TiO<sub>2</sub> single crystals and sintered electrodes: photoelectrochemical determination and comparative analysis, *J. Appl. Phys.* 55 (1984) 2977–2985.

- [15] A. Kay, I. Cesar, M. Grätzel, New benchmark for water photooxidation by nanosstructured  $\alpha$ -Fe<sub>2</sub>O<sub>3</sub> films, *J. Am. Chem. Soc.* 128 (2006) 15714–15721.
- [16] J. Luo, L. Steier, M.-K. Son, M. Schreier, M.T. Mayer, M. Grätzel, Cu<sub>2</sub>O nanowire photocathodes for efficient and durable solar water splitting, *Nano Lett.* 16 (2016) 1848–1857.
- [17] A. Kafizas, L. Francàs, C. Sotelo-Vazquez, M. Ling, Y. Li, E. Glover, L. McCafferty, C. Blackman, J. Darr, I. Parkin, Optimizing the activity of nanoneedle structured WO<sub>3</sub> photoanodes for solar water splitting: direct synthesis via chemical vapor deposition, *J. Phys. Chem. C* 121 (2017) 5983–5993.
- [18] W.-J. An, W.-N. Wang, B. Ramalingam, S. Mukherjee, B. Daubayev, S. Gangopadhyay, P. Biswas, Enhanced water photolysis with Pt metal nanoparticles on single crystal TiO<sub>2</sub> surfaces, *Langmuir* 28 (2012) 7528–7534.
- [19] K. Choy, Chemical vapour deposition of coatings, *Prog. Mater. Sci.* 48 (2003) 57–170.
- [20] A. Kafizas, I. Parkin, Materials for a sustainable future, *Glass and New Technologies*, 1st Edition, Cambridge, 2016, pp. 644–667.
- [21] V. Siriwongrungson, S.P. Krumdieck, M.M. Alkaissi, Conformality investigation of titanium dioxide thin films on 3-D micrometer-and nanometer-scale features by pulsed-pressure metal-organic CVD, *Chem. Vap. Deposition* 17 (2011) 327–336.
- [22] D. Lee, S. Krumdieck, S.D. Talwar, Scale-up design for industrial development of a PP-MOCVD coating system, *Surf. Coat. Technol.* 230 (2013) 39–45.
- [23] J. Walton, P. Wincott, N. Fairley, A. Carrick, Peak Fitting with CasaXPS, A Casa Pocket Book, 2010.
- [24] P. Swift, Adventitious carbon—the panacea for energy referencing? *Surf. Interface Anal.* 4 (1982) 47–51.
- [25] D. Nečas, P. Klapetek, Gwyddion: an open-source software for SPM data analysis, *Open Phys.* 10 (2012) 181–188.
- [26] M.C. Biesinger, L.W. Lau, A.R. Gerson, R.S.C. Smart, Resolving surface chemical states in XPS analysis of first row transition metals, oxides and hydroxides: sc, Ti, V, Cu and Zn, *Appl. Surf. Sci.* 257 (2010) 887–898.
- [27] A. Galuska, J. Uht, N. Marquez, Reactive and nonreactive ion mixing of Ti films on carbon substrates, *J. Vac. Sci. Technol. A: Vac. Surf. Films* 6 (1988) 110–122.
- [28] J. Morar, F. Himpel, G. Hollinger, J. Jordan, G. Hughes, F. McFeely, C 1 s excitation studies of diamond (111). I. Surface core levels, *Phys. Rev. B* 33 (1986) 1340.
- [29] A. Burke, C. Brown, W. Bowling, J. Glaub, D. Kapsch, C. Love, R. Whitaker, W. Moddemann, Ignition mechanism of the titanium–boron pyrotechnic mixture, *Surf. Interface Anal.* 11 (1988) 353–358.
- [30] A. Kafizas, X. Wang, S.R. Pendlebury, P. Barnes, M. Ling, C. Sotelo-Vazquez, R. Quesada-Cabrera, C. Li, I.P. Parkin, J.R. Durrant, Where do photogenerated holes go in anatase: rutile TiO<sub>2</sub>? a transient absorption spectroscopy study of charge transfer and lifetime, *J. Phys. Chem. A* 120 (2016) 715–723.
- [31] H.T. Grahn, *Introduction to Semiconductor Physics*, World Scientific Publishing Co Inc 1999, 2016.
- [32] K.M. Reddy, S.V. Manorama, A.R. Reddy, Bandgap studies on anatase titanium dioxide nanoparticles, *Mater. Chem. Phys.* 78 (2003) 239–245.
- [33] A. Ito, S. Nishigaki, T. Goto, A feather-like structure of  $\beta$ -Al<sub>2</sub>TiO<sub>5</sub> film prepared by laser chemical vapor deposition, *J. Eur. Ceram. Soc.* 35 (2015) 2195–2199.
- [34] A. Goossens, E.L. Maloney, J. Schoonman, Gas-Phase synthesis of nanostructured anatase TiO<sub>2</sub>, *Chem. Vap. Deposition* 4 (1998) 109–114.
- [35] Y. Takahashi, H. Suzuki, M. Nasu, Rutile growth at the surface of TiO<sub>2</sub> films deposited by vapour-phase decomposition of isopropyl titanate, *J. Chem. Soc. Faraday Trans. Phys. Chem. Condensed Phases* 81 (1985) 3117–3125.
- [36] I.S. Cho, Z. Chen, A.J. Forman, D.R. Kim, P.M. Rao, T.F. Jaramillo, X. Zheng, Branched TiO<sub>2</sub> nanorods for photoelectrochemical hydrogen production, *Nano Lett.* 11 (2011) 4978–4984.
- [37] W.-J. An, E. Thimsen, P. Biswas, Aerosol-chemical vapor deposition method for synthesis of nanostructured metal oxide thin films with controlled morphology, *J. Phys. Chem. Lett.* 1 (2009) 249–253.
- [38] W.-N. Wang, W.-J. An, B. Ramalingam, S. Mukherjee, D.M. Niedzwiedzki, S. Gangopadhyay, P. Biswas, Size and structure matter: enhanced CO<sub>2</sub> photo-reduction efficiency by size-resolved ultrafine Pt nanoparticles on TiO<sub>2</sub> single crystals, *J. Am. Chem. Soc.* 134 (2012) 11276–11281.
- [39] W. Leng, P.R. Barnes, M. Juozapavicius, B.C. O'Regan, J.R. Durrant, Electron diffusion length in mesoporous nanocrystalline TiO<sub>2</sub> photoelectrodes during water oxidation, *J. Phys. Chem. Lett.* 1 (2010) 967–972.
- [40] W. Zhou, X. Liu, J. Cui, D. Liu, J. Li, H. Jiang, J. Wang, H. Liu, Control synthesis of rutile TiO<sub>2</sub> microspheres nanoflowers, nanotrees and nanobelts via acid-hydrothermal method and their optical properties, *CrystEngComm* 13 (2011) 4557–4563.
- [41] R. Yang, Y.-L. Chueh, J.R. Morber, R. Snyder, L.-J. Chou, Z.L. Wang, Single-crystalline branched zinc phosphide nanostructures: synthesis, properties, and optoelectronic devices, *Nano Lett.* 7 (2007) 269–275.
- [42] D. Cao, G.-Q. Lu, A. Wieckowski, S.A. Wasileski, M. Neurock, Mechanisms of methanol decomposition on platinum: a combined experimental and ab initio approach, *J. Phys. Chem. B* 109 (2005) 11622–11633.
- [43] J. Liu, X. Yu, Q. Liu, R. Liu, X. Shang, S. Zhang, W. Li, W. Zheng, G. Zhang, H. Cao, Surface-phase junctions of branched TiO<sub>2</sub> nanorod arrays for efficient photoelectrochemical water splitting, *Appl. Catal. B: Environ.* 158 (2014) 296–300.
- [44] A.A. Tahir, T. Peiris, K. Wijayantha, Enhancement of photoelectrochemical performance of AACVD-produced TiO<sub>2</sub> electrodes by microwave irradiation while preserving the nanostructure, *Chem. Vap. Deposition* 18 (2012) 107–111.